Bone 118 (2019) 77–88

Contents lists available at ScienceDirect

Bone

journal homepage: www.elsevier.com/locate/bone

Full Length Article

Development of a 3D bone marrow adipose tissue model☆

Heather Fairfield [a,b,c,1], Carolyne Falank [a,b,c,1], Mariah Farrell [a,b,c], Calvin Vary [a,b,c], Joshua M. Boucher [a,b,c], Heather Driscoll [d], Lucy Liaw [a,b,c], Clifford J. Rosen [a,b,c], Michaela R. Reagan [a,b,c,*]

[a] Maine Medical Center Research Institute, Scarborough, ME 04074, USA
[b] University of Maine Graduate School of Biomedical Science and Engineering, Orono, ME 04469, USA
[c] Tufts University School of Medicine, Boston, MA 02111, USA
[d] Vermont Genetics Network, Department of Biology, Norwich University, 158 Harmon Drive, Northfield, VT 05663, USA

ARTICLE INFO

Article history:
Received 18 December 2017
Revised 16 January 2018
Accepted 17 January 2018
Available online 31 January 2018

Keywords:
3D
Bone marrow adipose
Tissue engineering
Silk scaffolds
Multiple myeloma

ABSTRACT

Over the past twenty years, evidence has accumulated that biochemically and spatially defined networks of extracellular matrix, cellular components, and interactions dictate cellular differentiation, proliferation, and function in a variety of tissue and diseases. Modeling *in vivo* systems *in vitro* has been undeniably necessary, but when simplified 2D conditions rather than 3D *in vitro* models are used, the reliability and usefulness of the data derived from these models decreases. Thus, there is a pressing need to develop and validate reliable *in vitro* models to reproduce specific tissue-like structures and mimic functions and responses of cells in a more realistic manner for both drug screening/disease modeling and tissue regeneration applications. In adipose biology and cancer research, these models serve as physiologically relevant 3D platforms to bridge the divide between 2D cultures and *in vivo* models, bringing about more reliable and translationally useful data to accelerate benchtop to bedside research. Currently, no model has been developed for bone marrow adipose tissue (BMAT), a novel adipose depot that has previously been overlooked as "filler tissue" but has more recently been recognized as endocrine-signaling and systemically relevant. Herein we describe the development of the first 3D, BMAT model derived from either human or mouse bone marrow (BM) mesenchymal stromal cells (MSCs). We found that BMAT models can be stably cultured for at least 3 months *in vitro*, and that myeloma cells (5TGM1, OPM2 and MM1S cells) can be cultured on these for at least 2 weeks. Upon tumor cell co-culture, delipidation occurred in BMAT adipocytes, suggesting a bidirectional relationship between these two important cell types in the malignant BM niche. Overall, our studies suggest that 3D BMAT represents a "healthier," more realistic tissue model that may be useful for elucidating the effects of MAT on tumor cells, and tumor cells on MAT, to identify novel therapeutic targets. In addition, proteomic characterization as well as microarray data (expression of >22,000 genes) coupled with KEGG pathway analysis and gene set expression analysis (GSEA) supported our development of less-inflammatory 3D BMAT compared to 2D culture. In sum, we developed the first 3D, tissue-engineered bone marrow adipose tissue model, which is a versatile, novel model that can be used to study numerous diseases and biological processes involved with the bone marrow.

1. Introduction

Bone marrow adipose tissue (BMAT) is a dynamic, endocrine adipose depot composed of bone marrow adipocytes (BMAs) as well as undifferentiated stromal cells, that has important roles in signaling with local bone marrow (BM) cells as well as distant cells. BMAT is responsive to many stimuli, including cold, PPARγ agonists (*e.g.*, rosiglitazone) [1], and diet [2,3]. In obesity, both BMAT and white adipose tissue (WAT) increase, while in other conditions, such as starvation/anorexia, these adipose depots respond oppositely: WAT decreases while BMAT increases, perhaps as an evolutionarily-selected adaptation to store energy reserves, or due to an inability to support hematopoiesis in the BM during starvation [4]. Thus, it is clear that BMAT is a unique adipose depot. In osteoporosis, obesity, and normal aging, BMAT volume increases [5]. Elevated BMAT leads to disrupted hematopoiesis, altered immune function, reduced bone mineral density, and uncoupling of the bone remodeling unit [6,7]. As we have shown, BMAT also increases in diet-induced obesity [2,8] and BMAT volume correlates with increased fracture risk in individuals with type 2 diabetes, anorexia nervosa, and other diseases [4,9–11]. Elevated BMAT may contribute to metabolic disorders or chronic systemic inflammation, or support tumor growth, and hence it is imperative to fully understand key factors

☆ Disclosure statement: The authors have nothing to disclose.

* Corresponding author at: Center for Molecular Medicine and Center for Translational Research, 81 Research Drive, Scarborough, ME, USA.
E-mail address: Mreagan@mmc.org (M.R. Reagan).

[1] Co-first authors.

https://doi.org/10.1016/j.bone.2018.01.023
8756-3282/

governing BM adipogenesis and adipocyte signaling [12–14]. Due to the great difficulty in uniquely studying the BMAT depot *in vivo*, accurately elucidating the roles of BMAT in healthy and diseased states requires controllable, tissue-engineered models of BMAT that allow for direct cell-cell contact and monitoring.

Understanding BMAT's role in cancer progression has great potential for the development of the next generation of anti-cancer therapies. Our lab hypothesizes that BMAT plays a role in bone-homing, osteolytic cancers such as multiple myeloma (MM) [15,16]. Adipocytes have been newly appreciated as a major constituent of the BM that can critically affect metastatic progression and drug resistance in prostate cancer and breast cancer, and potentially myeloma [6,17–22]. Interestingly, in acute myeloid leukemia (AML) clinical samples, a higher frequency of "small" BM adipocytes correlates with disease occurrence and drug resistance, suggesting that BM adipocyte shrinkage may accelerate tumor growth, chemoresistance, and relapse [23]. Elucidating how BM adipocytes influence tumor cell growth, behavior, and survival, and how tumor cells in turn affect BMAs, requires utilization of *in vitro* cell systems that mimic the physical and physiological microenvironment with high fidelity. Herein, we present novel three-dimensional (3D) culture approaches to study BMAs and model adipocyte–tumor cell interactions *in vitro*. We adapted our methods for constructing tissue engineered (TE)-WAT from human liposuction aspirates [24], and TE myeloma-bone models [25] to create the first *in vitro* BMAT 3D model, which we used to interrogate effects of myeloma on adipocytes.

2. Materials and methods

2.1. Silk scaffold preparation and cell seeding

Porous, aqueous 6.5% (wt/wt) silk fibroin scaffolds with pores of 500–600 μm were made following silk processing steps previously described [25,26], and cut into cylinders (5 mm by 3 mm height). Scaffolds were autoclaved and soaked in media containing 10% FBS and 1% PSF 1 day prior to seeding. Cells were seeded onto scaffolds at a density of ~1 × 10^6 cells per scaffold in ~20 μL of media; after 2 h, media was added to the wells to cover scaffolds. Cells were then expanded on scaffolds and switched to differentiation media when cells appeared evenly spread throughout the scaffold (~1–10 days after seeding scaffolds). For 2D culture comparisons, the same cells were seeded into wells and grown to similar confluency as observed in 3D culture before adipogenic differentiation media was added. All media and timing of media changes for 2D and 3D parallel cultures were identical, and staining and imaging was done with the same fixation procedure and staining solution.

2.2. Human bone marrow cell isolation, expansion and adipogenic differentiation

Primary human mesenchymal stromal cells (MSCs) were isolated from cancellous bone marrow from the acetabulum received from de-identified donors after total hip arthroplasty from men and women through the Maine Medical Center (MMC) Biobank. MMC IRB approval and informed consent was obtained for all human samples in accordance with the Declaration of Helsinki. MSCs were isolated by surface adherence as previously described [27]. Briefly, for each donor, ~3 mL of fresh, sterile BM was placed into a T-187.5 flask with hMSC expansion media consisting of Dulbecco's Modified Eagle's Medium (DMEM, Corning Inc.) supplemented with 10% FBS (Atlanta Biologicals, Flowery Branch, GA), 2 mM L-glutamine (Thermo Fisher Scientific, Waltham, MA), and 1× Antibiotic-Antimycotic (100 U/mL penicillin, 100 μg/mL streptomycin, 0.25 μg/mL fungizone) (Thermo Fisher Scientific). Media was added to BM cultures and hMSCs grown until 50% confluency was observed, and then floating cells were aspirated and hMSCs were expanded for use at passage 2–4. hMSC adipogenic media consisted of the basal hMSC media with 500 μM IBMX (VWR, Radnor, PA), 50 μM indomethacin (VWR), 1 μM dexamethasone (MilliporeSigma, Billerica, MA) and 1 μM insulin (VWR).

2.3. Mouse bone marrow cell isolation, expansion and adipogenic differentiation

To obtain whole mouse (C3H, KaLwRij or C57BL/6J) BM, tibia and femora dissected from mice were cut at both ends and placed into the tip of a 200 μL pipette that was then placed in a microcentrifuge tube and centrifuged at 200*g* for 2 min. Whole BM was then either seeded directly on scaffolds, or cultured in mouse MSC (mMSC) basal media (DMEM, 10% FBS and 1× Antibiotic-Antimycotic (100 U/mL penicillin, 100 μg/mL streptomycin, 0.25 μg/mL fungizone)) on tissue culture plastic to isolate mMSCs, which were expanded to passage 2–4 before being used. mMSCs were differentiated into adipocytes at two days post-confluence; adipogenic differentiation was induced with a 4-day treatment with induction media (basal media supplemented with 500 μM IBMX, 1 μM rosiglitazone (Cayman Chemical, Ann Arbor, MI), 1 μM dexamethasone, and 10 μg/mL insulin). This media was replaced with basal media supplemented with 10 μg/mL insulin and 1 μM rosiglitazone at day 4 and then maintained in basal media supplemented with 10 μg/mL insulin at day 7 and thereafter.

2.4. Multiple myeloma cell line culture

Multiple myeloma (MM) cell lines GFP^+/Luc^+MM1S, GFP^+/Luc^+5-TGM1, and $mCherry^+$/Luc^+OPM2 were provided by Dr. Irene Ghobrial (Dana-Farber Cancer Institute) and Dr. David Roodman (Indiana University) and cultured as previously described [28]. Media for MM cell expansion and co-culture with BMAT consisted of RPMI-1640 basal medium (VWR) containing L-glutamine media, 10% FBS, 1× Antibiotic-Antimycotic, and 1 μM insulin; diluted co-culture media was co-culture media diluted 1:1 with phosphate buffered saline (PBS, VWR). For myeloma cultures on BMAT or MSCs, mouse MSCs were seeded to silk and cultured until confluent and then switched to adipogenic media for 10 days or left in growth media. Then scaffolds were all switched to co-culture media and seeded with 0.5 × 10^6 myeloma cells (or no cells) and imaged over time.

2.5. Confocal microscopy imaging

For non-fixed, non-stained, non-invasive imaging, all samples were kept in media at 37 °C during imaging with a confocal microscope using the following settings: 10× objective, 2 frame averages, 405 nm (diode), 488 nm (argon) and 633 nm (HeNe) lasers, with emission detected with PMT1 (blue LUT, 417–458 nm), PMT2 (green LUT 510–572 nm) and HyD 3 (red LUT, 643–705 nm). For live-dead staining and imaging, samples were stained for 30 min at room temperature (RT) with 2 μM calcein AM (Thermo Fisher Scientific) and 4 μM ethidium homodimer-1 (Thermo Fisher Scientific), rinsed with PBS and imaged with confocal microscopy using the following settings: 10× or 20× objective, 405 nm (diode), 488 nm (argon) and 633 nm (HeNe) lasers, with emission detected with PMT1 (blue, ~460–480 nm) for autofluorescence of silk, PMT2 (green, ~510–550 nm) for live cells, and HyD3 (red, ~660–700 nm) for dead cells and ethidium homodimer bound to silk. For fixed adipocyte imaging, cells in 2D or 3D scaffold culture were fixed in 10% neutral buffered formalin (VWR) for 30 min at RT and then rinsed with PBS containing 0.2% Triton-X100 twice. Cells were then stained for 1 h with a working solution of PBS with 0.2% Triton-X100 (Thermo Fisher Scientific) containing 0.5 mg/mL Oil Red O (Amresco, Solon, OH), 20 units/mL Alexa Fluor 488 phalloidin (Thermo Fisher Scientific), and 100 ng/mL DAPI (Thermo Fisher Scientific) as we have previously described [24]. Cells were then rinsed twice with PBS and imaged on a confocal microscope using the following settings: 10× or 20× objective, excited with 405 nm (diode), 488 nm (argon) and 633 nm (HeNe) lasers, with emission

detected with PMT1 (blue, ~410–460 nm), PMT2 (green,~500–590 nm) and HyD 3 (red, ~646–700 nm). All confocal imaging was performed on scaffolds in 1.5 mm glass-bottomed dishes (MatTek Corporation, Ashland, MA) on a Leica SP5X laser scanning confocal microscope (Leica Microsystems, Buffalo Grove, IL) with Leica LAS acquisition software. Leica Application Suite Advanced Fluorescence (LAS AF) Lite software or Leica LAS acquisition software was used to make maximum projections of *Z*-stacks. Adipocyte diameter quantification was done using the length tool of the Leica Lite software. Diameters from all adipocytes in a field of view (FOV) were quantified using $n \geq 3$ FOVs per scaffold with $n = 3$ mice, analyzed with one-way ANOVA with Dunnett's multiple comparison testing (each compared to mBMAT alone control).

2.6. Total mRNA isolation, quantification and sample preparation and quality control for microarray

Whole BM from 16-week old littermate C57BL/6J mice (2 females and 3 males) was seeded onto 8 scaffolds/mouse (3D culture) or into one 24-well plate/mouse (2D culture) and cultured in mMSC expansion media. At day 12, adipogenic differentiation was induced. After 4 weeks, mRNA was isolated from whole 3D and 2D cultures for all 5 mice, and these 10 samples were used as biological replicates for microarray analysis. mRNA was isolated using QIAzol and miRNeasy isolation mini-kit with on-column DNase I digestion (Qiagen, Hilden, Germany) according to the manufacturer's protocol. Ribolock (Thermo Fisher Scientific) was added to inhibit RNA degradation for a final concentration of 1 U/μL. mRNA was quantified and tested for quality and contamination using a Nanodrop (Thermo Fisher Scientific) and subjected to quality control minimum standards of 260/230 > 2 and 260/280 > 1.8 prior to microarray library preparation.

2.7. Microarray

100 ng of total RNA was used to synthesize cDNA through a First-Strand reverse transcription reaction and Second-Strand RNA degradation reaction, using reagents from the GeneChip® WT PLUS Reagent Kit. cRNA was then synthesized through an overnight (16-hour) *in vitro* transcription reaction, which utilizes a T7 RNA polymerase. The cRNA was purified using an Affymetrix® magnetic bead protocol. Sample concentrations were determined using a 40 μg/mL/A260 constant on a Nanodrop1000 spectrophotometer. Approximately 15 μg of cRNA was then used to synthesize sense, single-strand cDNA using reagents from the GeneChip® WT PLUS Reagent Kit (any remaining cRNA template was hydrolyzed with RNase H). Single-stranded cDNA was purified using an Affymetrix® magnetic bead protocol. Sample concentrations were determined using a 33 μg/mL/A260 constant on a Nanodrop1000 spectrophotometer.

Approximately 5.5 μg of single-stranded cDNA was fragmented using UDG (10 U/μL) and APE1 (1000 U/μL), and labeled with biotin using TdT (30 U/μL) (GeneChip® WT PLUS Reagent Kit). Efficiency of the fragmentation and labeling reactions were verified using NeutrAvidin (10 mg/mL) with a gel-shift assay. Samples were combined with a hybridization mix, injected into Mouse Clariom S arrays, and placed in the Affymetrix® GeneChip® Hybridization Oven 645 at 45 °C and 60 rpm for 16.5 h. Arrays were stained using the Affymetrix® GeneChip® Fluidics Station 450 and scanned with the 7G Affymetrix® GeneChip® Scanner 3000.

2.7.1. Microarray data analysis

Raw data in the form of ten Affymetrix CEL files were imported into the Gene Expression Workflow in Partek Genomics Suite version 6.16.0701 (Partek, St Louis, MO). Background correction, quantile normalization, log2 transformation, and probeset summarization to transcript clusters/genes were performed using default settings for the Robust Multichip Average (RMA). Principal component analysis (PCA) was implemented using a covariance dispersion matrix as part of the data quality control. Differential expression between 3D and 2D culture was predicted at the gene-level (probe sets summarized into transcript clusters/genes). Two-way analysis of variance (ANOVA) was used to compare the gene expression data with respect to matrix type and subject ID (paired design, $n = 5$), with linear contrast 3D minus 2D. Multiple comparison correction was performed using Benjamini-Hochberg false discovery rate (FDR). Differentially expressed genes were defined based on an absolute fold change >2.0 in combination with an adjusted p-value with FDR < 0.05. Input for hierarchical clustering was RMA-normalized expression data standardized to a mean of zero and a standard deviation of one for the subset of DE genes with an absolute fold change >1.5 and FDR < 0.01.

In addition to differential expression at the individual gene level, we examined differential expression of functional groups or "disrupted" pathways using Pathway-ANOVA and GO-ANOVA as implemented in Partek. Both Pathway- and GO-ANOVA were performed on the normalized data directly without any filtering using the Method of Moments algorithm. Parameters for the Pathway- and GO-ANOVA analyses were configured such that only pathways with more than two and fewer than 500 genes are considered and only GO-terms with more than two and fewer than 100 genes were considered. Both raw intensity data (.CEL files) and RMA-normalized expression values are available in the National Center for Biotechnology Information Gene Expression Omnibus (NCBI GEO) Series accession no. GSE108374 (https://www.ncbi.nlm.nih.gov/geo/query/acc.cgi?acc=GSE108374).

2.7.2. Gene set enrichment analysis (GSEA)

Microarray data were also analyzed by GSEA (gene set enrichment analysis) using the Java implementation available from the Broad Institute (http://software.broadinstitute.org/gsea/index.jsp). RMA-normalized expression values from Clariom S Mouse array probesets were used as input and were converted to gene symbols for the GSEA. Several Molecular Signatures Database (MSigDB) Collections were used to identify gene sets significantly enriched in 3D *vs* 2D cultures, including H (Hallmark), C2 (curated gene sets) and C5 (Gene Ontology, GO, gene sets) (http://software.broadinstitute.org/gsea/msigdb/collections.jsp). Gene set size filters ($min = 15$, $max = 500$) were applied and 'Signal2Noise' was used for the gene ranking metric. Only those gene sets with a false discover rate (FDR) <25% were considered significantly enriched.

2.8. Mass spectrometry and proteomics

For mass spectrometry in the MMCRI Proteomics and Lipidomics Core Facility, 3D and 2D BMAT samples were derived from mMSCs from male C57BL/6J mice aged 5–7 months and differentiated for 1 month in adipogenic media. These whole samples were also compared to aged-matched primary *ex vivo* brown (interscapular) adipose tissue and white (gonadal) adipose tissue. For protein isolation for MS/MS analysis, whole fresh samples were lysed on ice by grinding with a micro-tube pestle in the presence of RIPA supplemented with protease/phosphatase inhibitor cocktail (cat# 5872S Cell Signaling Technologies, Danvers, MA), followed by sonication for 10s at 30% duty cycle. Lysates were centrifuged at 14,000*g* for 10 min to pellet insoluble debris and the supernatants were transferred to new tubes. Proteins were precipitated using 4-volumes of ice-cold acetone and incubated at −20 °C overnight. The following day, samples were centrifuged at 10,000*g* for 15 min to pellet the precipitated protein. The remaining acetone solution was poured off and the pellets were re-suspended in ice-cold 70% acetone to wash, and centrifuged at 5000*g* for 5 min to pellet. Acetone solution was poured off and the pellets dried for ~30 min at room temp with the caps open. To resuspend proteins, RIPA containing 1% SDS with protease/phosphatase inhibitor was added to each pellet, and triturated up and down repeatedly to break apart. The pellets

were vortexted to re-solubilize protein, sonicated on ice for 10s at 30% duty cycle, and submitted for trypsin-based peptide fragmentation.

Tryptic digests were performed using the ProteoExtract digestion kit (Calbiochem, Darmstadt, Germany). Tryptic peptides were separated on a Ultimate RSLC system 3000 (ThermoFisher/Dionex) nanoscale liquid chromatograph and infused onto a 5600 TripleTOF mass spectrometer (Sciex, Framingham, MA). Sequential Window Acquisition of all Theoretical Spectra (SWATH) was used to profile all proteins using a data-independent acquisition method [29]. A human-specific ion library comprising 4091 proteins was constructed using ProteinPilot software (Sciex). For identification of peptides, multiple fragment ion chromatograms were retrieved from the spectral library for each peptide of interest. These spectra were compared with the extracted fragment ion traces for the corresponding isolation window to identify the transitions that best identify the target peptide. SWATH analysis was performed using Sciex PeakView software, and Sciex MarkerView software was utilized for **principal** component analysis and *t*-test comparisons. FC > 2 or <0.5, $p < 0.05$ identified proteins significantly different between 2D and 3D samples.

2.9. Statistical analysis

All data are expressed as mean ± standard deviation (SD), unless otherwise noted. Student's t-test, ordinary one-way or two-way ANOVA tests were used to determine significance, using $p < 0.05$ as the cut-off, with Tukey's multiple comparison post-hoc testing unless otherwise noted. ****$p < 0.0001$; ***$p < 0.001$; **$p < 0.01$; *$p < 0.05$. Prism 6.02 software was used to compute all statistical calculations unless otherwise noted.

3. Results

3.1. Silk scaffolds support mouse and human tissue engineered BMAT

In preliminary studies, we performed a variety of cultures with different types of adipocytes in 3D silk scaffolds to validate their support of adipocyte culture, such as our primary mouse osteocyte 2 day co-culture with differentiated 3T3-L1 mouse adipocytes. We also co-cultured human lipoaspirate WAT, previously described [24], with MM1S myeloma cells and observed that the myeloma cells as well as lipoaspirate cells were viable for 2 weeks (data not shown). Building on our optimization of culturing and staining procedures, we next developed our 3D tissue engineered (TE)-BMAT mouse models. Using whole mouse BM seeded directly onto silk scaffolds, we observed that the scaffolds supported adherent stromal marrow cell viability, uniform distribution, proliferation and adipogenic differentiation (Fig. 1). Initially, BM cells displayed a spherical phenotype, and many were non- or weakly-adherent (Fig. 1A). By day 7, cells began to flatten, elongate, take-on a fibroblastic phenotype, and stretch across the scaffold pores (Fig. 1B). On day 10, cells were switched to adipogenic media and at day 14 of culture (day 4 adipogenic differentiation), more fibroblastic-like and fewer round cells were observed, and yellow/orange autofluorescent spheres from lipids were visible (Fig. 1C). At day 11 of adipogenesis, multilocular and unilocular adipocytes had developed (Fig. 1D) and at day 16 of adipogenesis, most adipocytes appeared to be unilocular (Fig. 1E, F). This work validated that our BM collection, scaffold-seeding, and culture process successfully isolated a heterogeneous population of cells, including stem cells that retained their capacity to undergo adipogenic differentiation. A second model was also generated where mouse BM stroma was isolated, passaged *in vitro* in 2D, and then seeded onto silk

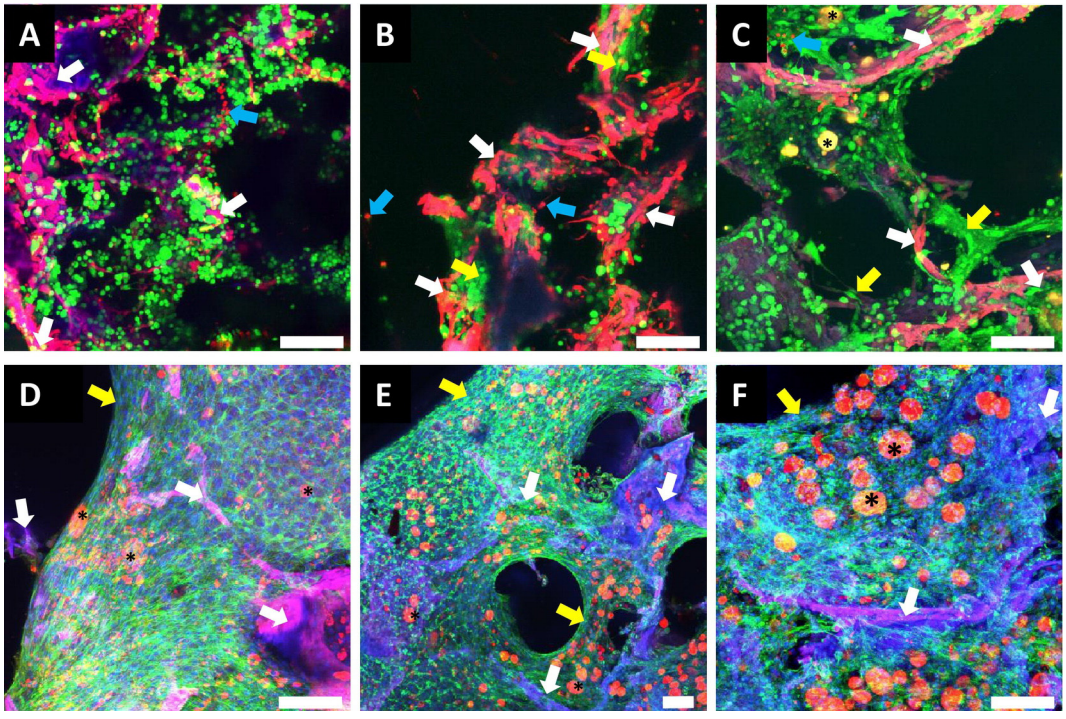

Fig. 1. Development and characterization of 3D mouse bone marrow adipose tissue derived from whole bone marrow using confocal microscopy. A) C3H mouse whole BM was seeded onto silk scaffolds and confocal imaged at day 3, 7, 14, 21, and 26. Scaffold is autofluorescent in every channel and appears purple/pink. A–C) Live dead imaging shows live cells are green with calcein AM stain and dead cells are red with ethidium homodimer-1. A) Day 3 of culture: most cells are alive (green) with a round morphology. B) Day 7 of culture: live cells have an elongated, mesenchymal morphology rather than rounded, and they are located along the scaffold. C) Day 14 culture (day 4 adipogenic differentiation) live-dead imaging. More fibroblastic-like and fewer round cells were observed. Yellow/orange spheres indicate autofluorescence from lipids. D–F). Fixed scaffolds stained with Oil Red O (lipids, red), phalloidin (actin, green), and DAPI (nuclei, blue). Scaffold is autofluorescent (maroon). Both adipocytes and undifferentiated stromal cells are observed throughout the scaffold. D) Day 21 culture, day 11 adipogenesis. E, F) Day 26 culture, day 16 adipogenesis. Scale bar = 100 μm. White arrows indicate scaffold; blue arrows indicate dead cells; yellow arrows indicate stromal cells; asterisks indicate adipocytes.

scaffolds and differentiated in adipogenic media; resulting BMAT models could not be differentiated from BMAT models created by seeding fresh, whole BM directly to scaffolds. Interestingly, we observed that, even without fixation and staining with Oil Red O, lipid droplets could be identified based on autofluorescence, observed in the red channel (660–700 nm) (Fig. 1C). Future research will investigate and further explore this phenomenon. We also demonstrated long-term stability of mouse BMAT (mBMAT) models using confocal imaging of 3D BMAT after 3 months of adipogenic differentiation using BM from 2 different mouse strains (Supp Fig. 1).

We next developed a human tissue-engineered 3D BMAT model. Human MSCs were isolated from BM aspirates, expanded *in vitro* in 2D, seeded onto scaffolds, and imaged at days 1 and 9 using non-destructive, live-dead imaging and days 10 and 28 using Oil Red O, DAPI and phalloidin staining of fixed scaffolds (Fig. 2). MSCs proliferated throughout the scaffold and few red (dead) cells were visible, as most of these detach and float away from the scaffold (Fig. 2A, B). By day 10, lipid accumulation was observable in many cells and, as with mouse samples, many stromal cells did not differentiate into adipocytes (Fig. 2C). Interestingly, we observed a species dependence of BMAT locularity: while mouse BMAT was unilocular at day 26, human BMAT (hBMAT) consisted of multilocular adipocytes even at day 28 (Fig. 2D). Our model thus captures the heterogeneity of BM stromal cells, which include stem cells/BM adipocyte progenitors as well as stromal cells unable to undergo adipogenesis.

3.2. Silk scaffolds support C57BL/6J 3D-BMAT and demonstrate significant differences versus 2D in gene expression via microarray

We then characterized differences between 2D and 3D mBMAT samples on the genetic level. BM from 5 C57BL/6J male and female mice was isolated and seeded into 3D or 2D culture and cultured as described in Fig. 1. We validated successful BM isolation, scaffold seeding, expansion of BMSCs on scaffolds, and differentiation into adipocytes in adipogenic media using confocal live/dead and Oil Red O/DAPI/phalloidin imaging (Supp Fig. 2). After 28 days of adipogenesis, total RNA from matched 3D and 2D samples was harvested and analyzed using microarray analysis. PCA multivariate analysis of all 22,206 genes in the microarray found a strong distinction between 2D and 3D samples (Fig. 3A). 81 genes passed a two-way ANOVA with a strict FDR 0.01/fold change > 2 filter; these are plotted as a heat map (Fig. 3B). To better interpret gene expression changes, Pathway-and GO-ANOVA analyses were performed to identify KEGG pathways and GO categories that are significantly different. Out of 275 KEGG pathways, 60 were upregulated (Supp Table 1) and 69 were downregulated (Supp Table 2) in 3D and 3D with $p < 0.0001$ using Pathway-ANOVA. In 3D culture, normal metabolic, ribosome, protein, and proliferation pathways were upregulated, such as DNA replication, ribosome, cell cycle, and biosynthesis and metabolism pathways. In contrast, many inflammatory, disease-related, and cytokine-associated pathways were upregulated in 2D cultures, such as NOD-like receptor signaling pathway, malaria, prion disease,

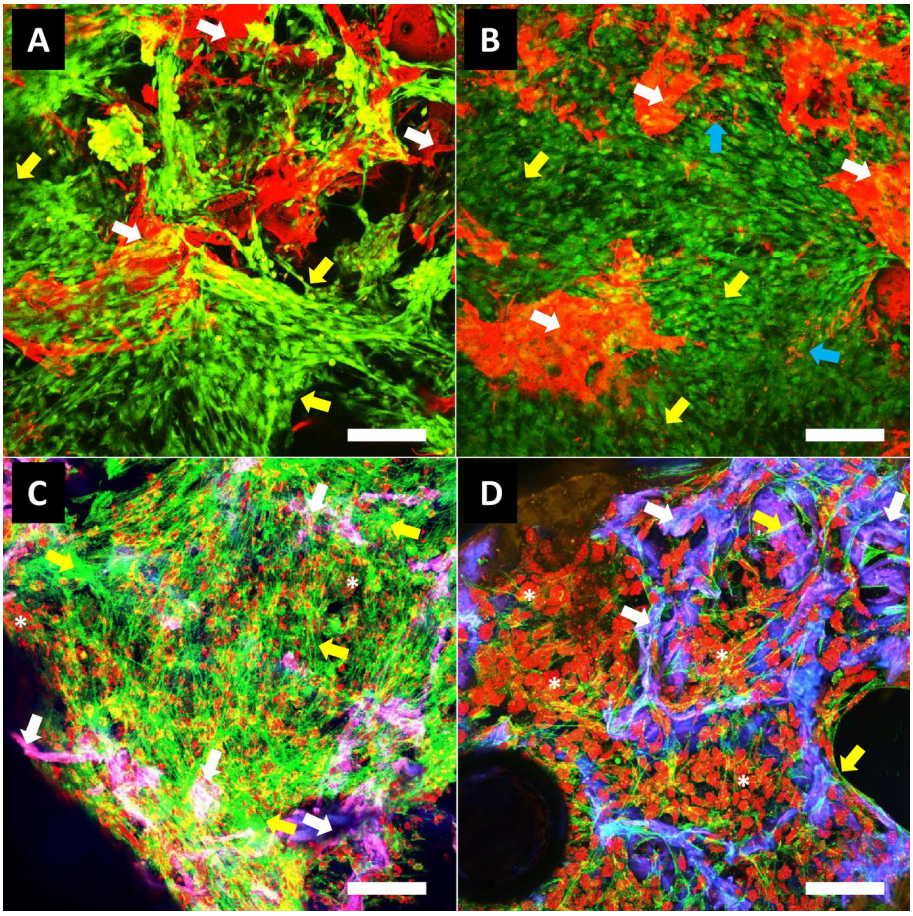

Fig. 2. Development and characterization of 3D human bone marrow adipose tissue derived from hMSCs. A–B) Live dead imaging shows live cells are green with calcein AM stain and dead cells are red with ethidium homodimer-1, (A) Day 1 and (B) Day 9 (day 8 of adipogenesis) (B) after hMSC seeding. C–D) Fixed scaffolds stained with Oil Red O (lipids, red), phalloidin (actin, green), and DAPI (nuclei, blue). Scaffold is autofluorescent (red or maroon). Both adipocytes and undifferentiated stromal cells are observed throughout the scaffold. C) Day 10 (day 9 of adipogenesis). D) Day 28 (day 27 of adipogenesis). Scale bar = 200 μm. Representative images from n = 4 different hMSC donors. White arrows indicate scaffold; blue arrows indicate dead cells; yellow arrows indicate stromal cells; asterisks indicate adipocytes.

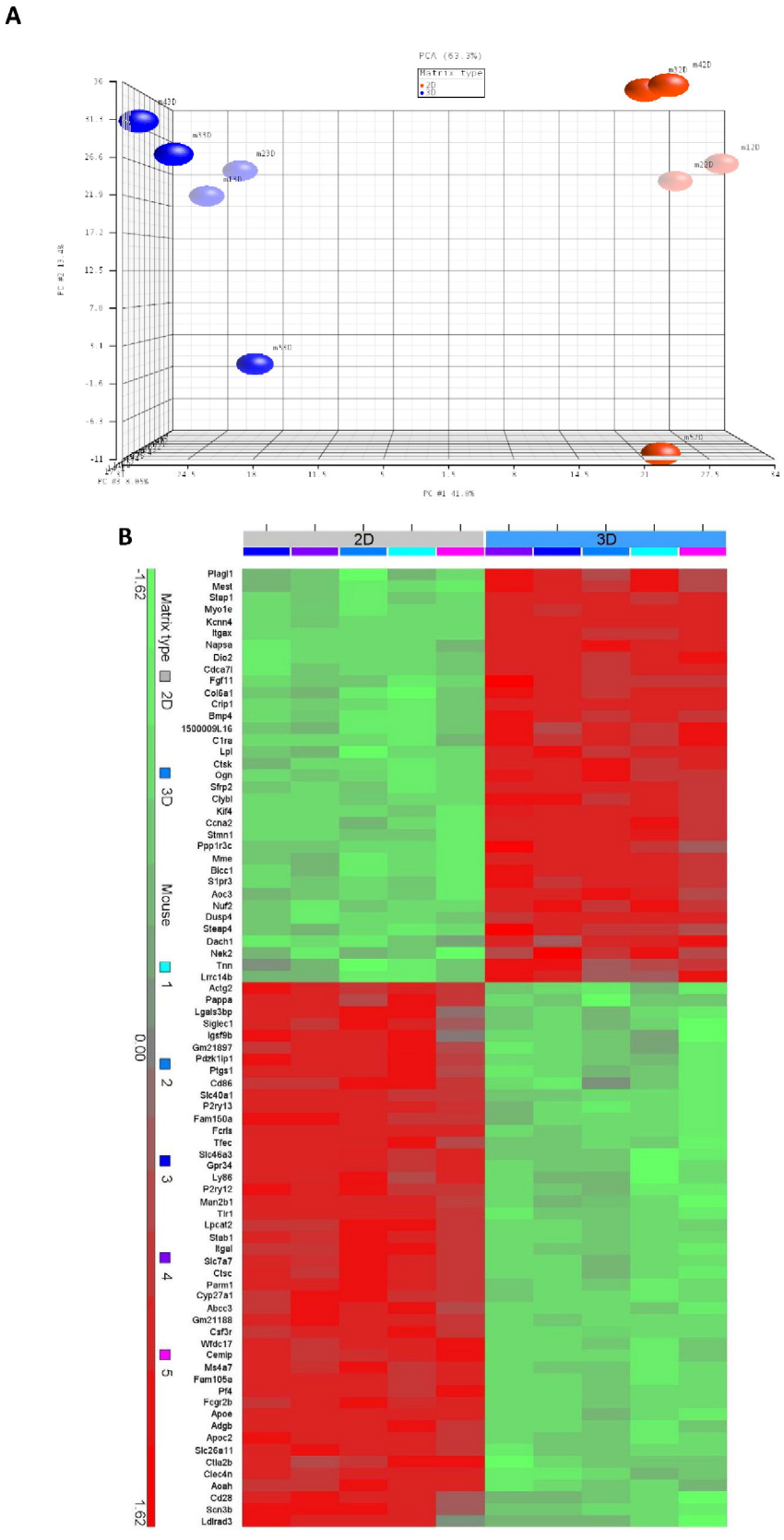

Fig. 3. Microarray gene expression analysis of 2D *versus* 3D mouse BMAT. A) Principal component analysis (PCA), a multivariate, unbiased analysis, demonstrates distinct grouping of samples from 2D (red) and 3D (blue) mBMAT. PC1 correlated with culture conditions (3D *vs* 2D) demonstrating the significant impact of 3D culture. B) Microarray heat map showing hierarchical clustering of the 81 genes that passed the FDR < 0.01 and fold change>2 filter. The heat map color scale is reflective of the standardized normalized expression data input, which was standardized to a mean of zero and a standard deviation of one. Red indicates overexpression and green indicates underexpression.

TNF signaling, and other infection and disease pathways. Fifteen MSigDB Hallmark gene sets were also found to be significantly enriched in 3D *versus* 2D cultures (Table 1). Similarly, of the 14,677 GO categories, 178 were significantly upregulated (Supp Table 3) and 146 were significantly downregulated (Supp Table 4) in 3D *vs* 2D culture ($p < 0.0001$, $FC > 1.5$). The top most upregulated GO terms had to do with cell proliferation, differentiation, growth factor response, extracellular matrix secretion, and pattern specification/polarity. The top downregulated GO terms were centered on disease pathways (Toll-like receptor and COX/COX2 pathways) and lipoprotein related pathways. Overall, Pathway- and GO-ANOVA indicated that 3D culture supported less inflammatory adipocyte phenotype compared to the same cells in 2D culture.

3.3. Proteomics analysis of 2D BMAT, 3D BMAT and primary adipose tissue

Interestingly, we also saw significant differences between 3D and 2D mBMAT samples through large-scale proteomic analyses. Analysis of 4 male mouse BMAT samples grown in 2D or 3D was performed using mass spectrometry and PCA analysis (Fig. 4, purple and green dots). A clear distinction between 2D and 3D BMAT was evident and 136 proteins were significantly different between these groups: 92 proteins were up-regulated and 44 proteins were down-regulated in 3D *vs* 2D culture (Supp Table 5). We also compared BMAT samples to freshly isolated brown and white adipose tissue from age and sex-matched C57BL/6J mice, using SWATH analysis and PCA (Fig. 4, blue and red dots) and observed clear sample clustering by PCA. The protein compositions of the two primary, uncultured adipose depots were more similar to each other than to 2D or 3D BMAT, and BMAT protein composition was unique and located between WAT and BAT samples along the **principal** component 2 axis. Due to the challenges in obtaining pure, fresh BMAT, the comparison between mouse BMAT and 3D BMAT cultures could not be performed, but future directions will interrogate ways to isolate pure BM adipocytes for this purpose.

3.4. 3D hBMAT supports myeloma and displays delipidation response to myeloma

We then attempted to create a human BMAT-myeloma co-culture model, building on our previous model of 3D WAT [30] and our findings that BMAT may affect myeloma cells [21], to explore complex adipose-myeloma interactions [31]. We created 3D hBMAT-myeloma co-cultures and observed that 3D hBMAT successfully supported MM1S growth for 3 weeks (Fig. 5). Undifferentiated stromal cells within the 3D hBMAT appeared to be reduced by MM1S cells, similar to previous findings from our lab and others showing apoptosis and senescence induced in myeloma-associated BM mesenchymal stroma (yellow arrows, Fig. 5) [32,33]. BM adipocytes co-cultured with myeloma cells appeared less healthy than in the tumor-free, healthy controls as indicated by the presence of extracellular lipids (red droplets outside of cells) and decreased actin visualized around adipocytes at all times (Fig. 5). After 3 weeks, few MM1S cells were present on the scaffold alone, but many were observed in hBMAT scaffolds (white arrows, Fig. 5), and very few stromal cells remained in the co-cultures. To quantify changes in BMAT in response to myeloma cells, we next developed a mouse BMAT-myeloma model, which increased the reproducibility and controllability of our findings and removed confounding effects of human donor MSC differences.

Table 1
Gene set enrichment analysis summary of all significant pathways.

Hallmark pathway name-upregulated in 3D	Enrichment score	Normalized enrichment score	FDR q-val
mTORC1 Signaling	0.4157092	1.5615747	0.19567661
Glycolysis	0.5289566	1.5271125	0.16126063
MYC Gene Targets (v1)	0.53750265	1.5176365	0.11344414
Unfolded Protein Response	0.4240947	1.4877199	0.110531986
Hypoxia	0.53257245	1.4775536	0.09381858
Oxidative Phosphorylation	0.30532646	1.4505394	0.10814332
Adipogenesis	0.4223209	1.4470688	0.09784364
DNA Repair	0.29531318	1.4233307	0.11807318
G2M Checkpoint	0.66986865	1.4173219	0.11180904
Mitotic Spindle	0.49542296	1.3993406	0.1314721
MYC Gene Targets (v2)	0.42623973	1.3975677	0.12237608
E2F Transcription Factor Targets	0.69179046	1.3961971	0.11492941
Wnt/Beta-Catenin Signaling	0.40139306	1.3566543	0.15412405
Ultraviolet (UV) radiation response (down-regulated)	0.36637568	1.3167368	0.19206767
Spermatogenesis	0.4566163	1.2831532	0.22546245

Note: No significant pathways were identified in the 2D samples using GSEA.

3.5. 3D mBMAT supports myeloma and displays delipidation in response to myeloma

We then tested our capacity to culture myeloma cells on 3D mouse BMAT (mBMAT) and assessed the response of mBMAT to myeloma cells to better understand the myeloma-BMAT relationship. As with hBMAT, adipocytes and undifferentiated stromal cells were observed throughout the 3D mBMAT, but in co-culture, there appeared to be fewer BM stromal cells and, surprisingly, reduced adipocyte lipid content in mBMAT samples after 1 week co-culture with myeloma cells (Fig. 6A, B). These findings persisted after 2 weeks of co-culture (data not shown). MSCs also appeared to be decreased in the 3D model when co-cultured with myeloma cells (Fig. 6A), demonstrating destruction of the BM niche characteristic of myeloma [25,34]. While few GFP^+/Luc^+5TGM1 cells adhered to scaffolds alone, many were evident on 3D BMAT and on MSC cultures after 1 week in culture (data not shown).

To quantify the myeloma-induced delipidation, 3D mBMAT samples were cultured with GFP^+/Luc^+MM1S or GFP^+/Luc^+5TGM1 cells for 2 weeks in regular or diluted media (to stimulate a stressed state), and stained with Oil Red O, Alexa Fluor 568 phalloidin, and DAPI. Samples were then confocal imaged using *Z*-stack, maximum projection images. Adipocyte diameter was significantly reduced in BMAT when cultured with both cell types in either media, indicating that myeloma cells reduce BMA lipid content (Fig. 6B). mBMAT was also able to support OPM2 myeloma cells for 2 weeks *in vitro*, although the reduction in lipids in BMAs was not as evident with these myeloma cells (data not shown). The mechanisms by which delipidation and changes in BMAT occur remain to be interrogated and may include dedifferentiation, transdifferentiation, lipid release, lipid utilization, senescence, lipophagy, or cell death. Importantly, the consequences of these changes in adipocytes on myeloma cells may be profound and may contribute to BMAT-induced drug resistance we have recently reported [21].

We also validated that C57BL6J/KaLwRij mouse BMSCs could be differentiated into adipocytes on scaffolds and support GFP^+/Luc^+5TGM1 tumor cell culture (Fig. 6C). Interestingly, some, but not all, GFP^+/Luc^+5TGM1 cells were found to contain lipid droplets after 1 week in co-culture with mBMAT, which has not been observed by us or ever reported in GFP^+/Luc^+5TGM1 cells alone, suggesting the potential for lipid transfer from adipocytes to tumor cells in parallel with destruction of BMAs. Lipid accumulation within OPM2 cells was also observed after 1 week in co-culture with C57BL/6J-derived mBMAT, and this appeared especially prominent in tumor cells closely associated with adipocytes compared to OPM2 cells more distant from adipocytes (data not shown).

4. Discussion

Our work has contributed to the field of tissue engineering through development of a tissue engineered bone marrow adipose model. Tissue engineered organs have become increasingly utilized in *in vitro* disease modeling to better recapitulate the *in vivo* environment in which cells grow. In numerous organs, scaffolds, and model systems, increasing evidence demonstrates that scaffold stiffness, geometry, chemistry and spatial dimensionality, as well as the composition of neighboring cells

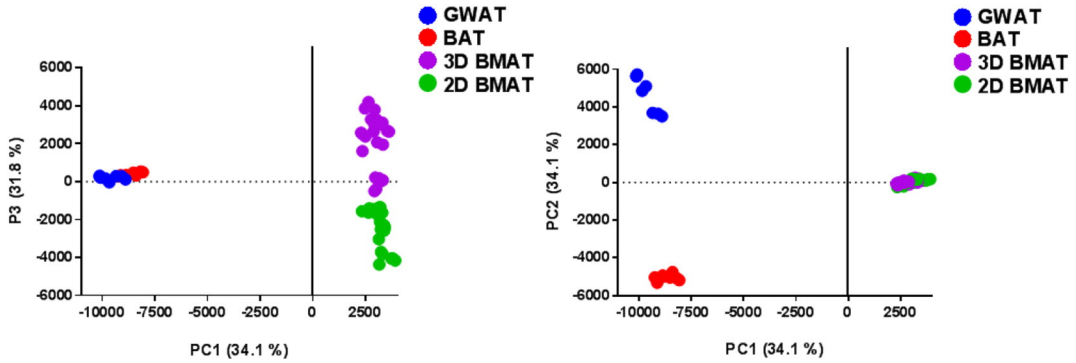

Fig. 4. Proteomic analysis of 3D *vs* 2D BMAT. Mass spectrometry and proteomic analysis was performed on 2D and 3D mBMAT. Normalized Principal Component (PC) Analysis (PCA) (PC 1 *vs* PC 2, and PC 1 *vs* PC 3) of 2D and 3D BMAT samples *versus* primary adipose depots (GWAT, gonadal white adipose tissue, and BAT, brown adipose tissue) demonstrates distinct grouping based on adipose origin and also a distinction between 3D and 2D BMAT. N ≥ 3 scaffolds or wells were combined together per biological replicate and n = 4 biological replicates (individual mice) were used. N = 5 technical repeats per sample were used. D1 represents PC 1, D2 represents PC 2, and D3 represents PC 3.

and biochemical signaling factors, regulate cellular migration, differentiation, and behavior, leading to differences in tissue formation and function [35]. Cell proliferation, metabolism, gene expression, protein synthesis, and drug metabolism/resistance are substantially altered, and are typically much more physiologically accurate, in 3D scaffolds compared to 2D cultures [25,36–42]. We have similarly found that 3D models are better models of healthy BMAT, suggesting that these models will accelerate the translation of preclinical research by more accurately predicting disease course, responsive subpopulations, or treatment responses.

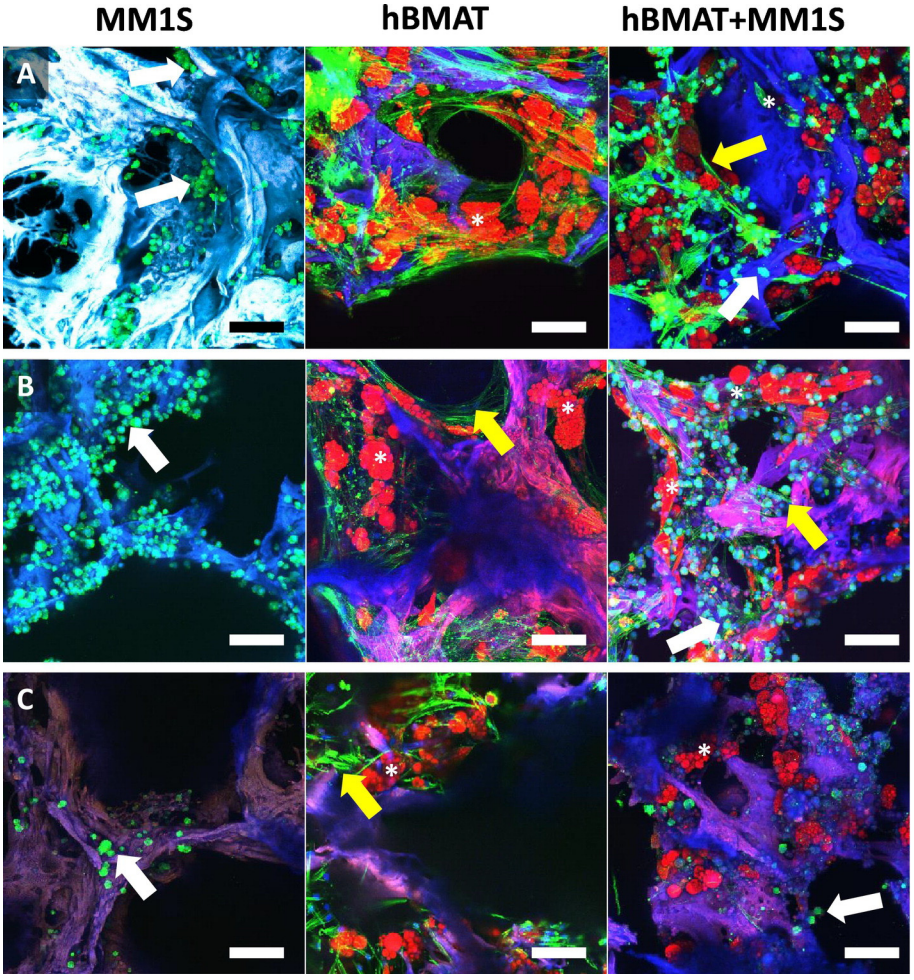

Fig. 5. Human BMAT co-culture supports MM1S myeloma cells. Maximum projections of confocal imaging of co-cultures. hBMAT was seeded to silk, cultured until confluent and then switched to adipogenic media for 37 days. Then scaffolds were switched to a co-culture media and seeded with GFP^{+}/Luc^{+}MM1S cells and imaged at 1 week (A), 2 weeks (B) or 3 weeks (C). Fixed scaffolds were stained with Oil Red O (lipids, red), phalloidin (actin, green), and DAPI (nuclei, blue). Scaffold is autofluorescent (maroon). Both adipocytes and undifferentiated stromal cells are observed throughout the BMAT and negatively impacted by myeloma cells. Scale bar = 100 μm. White arrows indicate tumor cells; yellow arrows indicate stromal cells; asterisks indicate adipocytes.

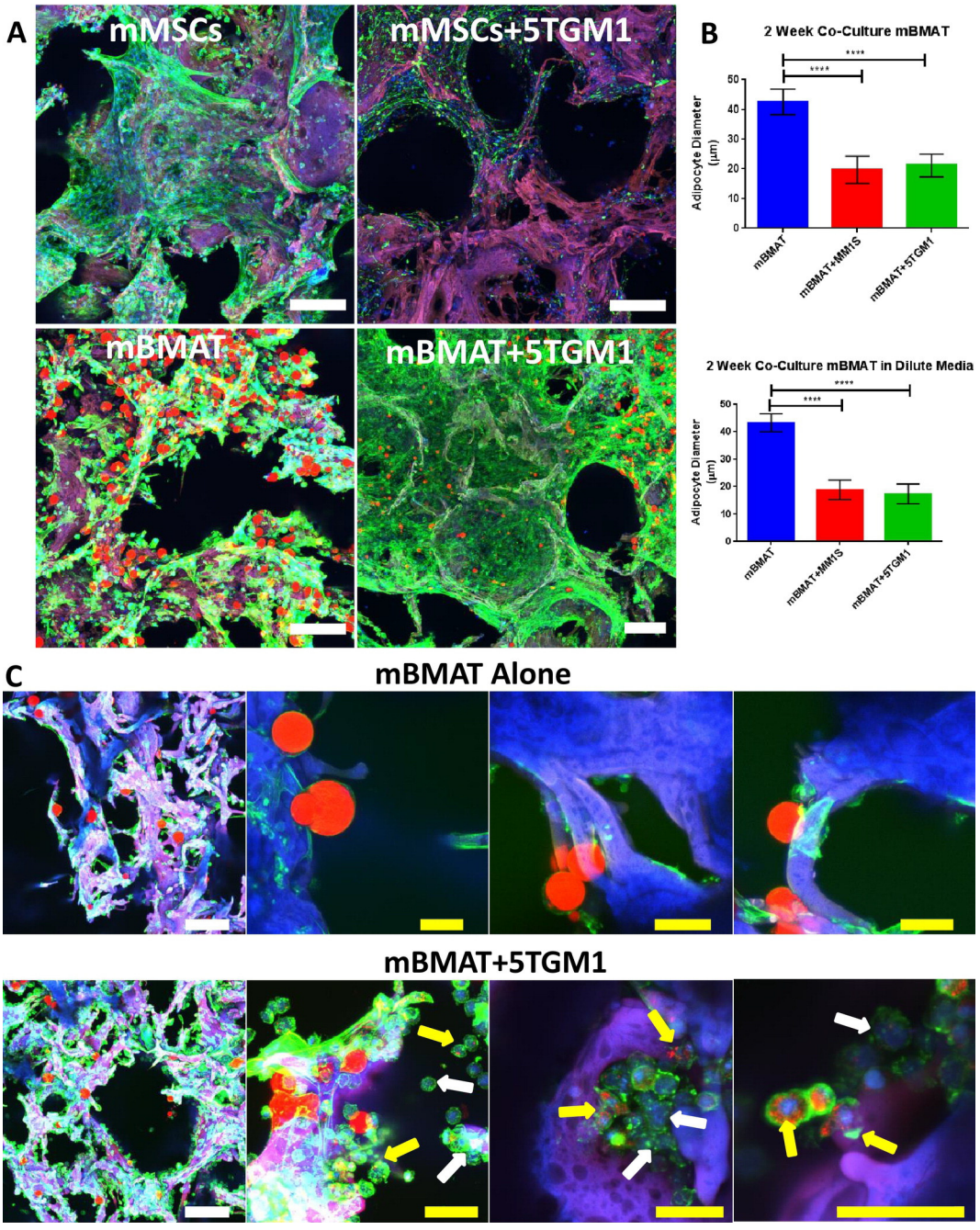

Fig. 6. mBMAT and mMSC co-cultures support 5TGM1 and MM1S myeloma cells. Maximum projections of confocal imaging of scaffolds fixed and stained with Oil Red O (lipids, red), phalloidin (actin, green), and DAPI (nuclei, blue). Scaffold is autofluorescent maroon/blue. A) mMSCs and mBMAT (derived from C57BL/6J mMSCs expanded *in vitro* and seeded to scaffolds) after 1 week culture or co-cultures with GFP^+/Luc^+5TGM1. Lipid content and stroma cell count appeared decreased in BMAT when co-cultured with myeloma cells. B) Quantification of BMAT adipocyte diameter after 2 week culture with GFP^+/Luc^+5TGM1 or GFP^+/Luc^+MM1S in co-culture or diluted media. Data represented as mean ± SEM, n = 9 (n = 3 mice per group, n = 3 scaffolds per mouse). C) C57BL6/KaLwRij-derived MSC differentiation into 3D BMAT after 11 days of adipogenesis and cultured alone (top) or co-cultured with GFP^+/Luc^+5TGM1 cells (bottom) for 1 week. Interestingly, some myeloma cells contained small lipid droplets (yellow arrows), but most did not (white arrow). Representative images from n = 2 mice with n = 6 scaffolds per mouse for monoculture and co-culture. White scale bar = 200 μm; yellow scale bar = 50 μm.

Specifically for adipose tissue, 3D models are invaluable. Studies of adipose tissue biology are conducted primarily in monolayer, cell suspension or ceiling cultures [43–47]. However, 3D, adherent cultures have proven necessary for accurate modeling [48], as these other systems often do not translate well to human adipocyte function [49] (*e.g.*, cells often secrete subphysiologic levels of adipokines or display a fibroblast-like rather than round, unilocular phenotype [44,47,48,50–52]). Biocompatible, porous silk scaffolds allow for nutrient transport, cell adhesion, require no chemical crosslinking, and have already proven useful for WAT modeling [53–55]. Our 3D BMAT model utilized durable silk scaffolds, which provided mechanical robustness and an accurate spatiotemporal microarchitecture to accurately model the BM adipose depot. 3D, tissue engineered BMAT supported long-term culture and adipogenic differentiation of MSCs and better recapitulated healthy, normal conditions than 2D cultures. Moreover, as investigating the BMAT depot *in vivo* is incredibly challenging, since it

is physically difficult to access and biochemically very complex to specifically target, scientists will greatly benefit from our *in vitro* BMAT models for physiology or pathophysiology research.

Additionally, our 3D BMAT model enabled longitudinal investigation of myeloma cultures in BMAT in physiologically-relevant conditions. 3D modeling for tumors is critical for accurately studying tumor biology; the substrate modulus of a tissue surrounding a tumor dramatically affects cell behavior, gene expression, phenotype and invasion potential [56,57]. Other groups have described 3D hydrogel cultures of BMAs and prostate cancer cells [58], but ours is this is the first scaffold-based 3D BMAT or BMAT-tumor co-culture model. Our model can be used to study mechanical and chemical signals over multiple length and time scales that direct how tumor cells integrate into the local BM niche, evolve, become drug resistant, and induce osteolysis [59]. These models have the potential to support drug screening, accelerate personalized medicine through patient-specific models, and identify novel biomarkers or therapeutic treatments to improve clinical outcomes.

Although our model can be used to co-culture BMAT with any other cell type, we wanted to investigate myeloma cells due to the many associations, but lack of a well understood relationship, between these cells. BMAT is elevated with aging and obesity, and these states also correlate with increased myeloma risk [16,19,60–62]. BM transplant, a common treatment for MM, requires BM irradiation which induces massive BMAT expansion that could play a large role in the reemergence of drug-resistant clones. Moreover, other labs have found that BM adipocytes can support on myeloma cells and that BMAT-derived bioactive lipids and adipokines (*e.g.*, leptin) may promote metastasis [63–65]. Correlations between BMAT and myeloma thus support greater scientific inquiry into the cross-talk between these cells.

We were intrigued to see decreased lipids within BMAT cultured with myeloma cells. Acute myeloid leukemia (AML) patients have more small BM adipocytes compared to normal controls, and small BMAs predict poor prognosis [23]. Middle- and large-size adipocytes were fewer in number in AML samples, although that change was not significant. The authors also verified that adipocyte size change was not caused by a lack of space due to excessive invasion of leukemia cells [23]. They hypothesized that resultant changes in free fatty acids and AML-secreted GDF15, a TGFβ family member, may facilitate changes in BMA-tumor cell communication. Small adipocytes may also have higher metabolic activity, but this remains to be explored. We hypothesize that despite a potential dependency on BMAs, myeloma cells may decrease the BMA lipid content to fuel their own growth in a temporally-regulated manner; the specifics of how this occurs remain to be determined. Uncovering the mechanisms involved in delipidation will be crucial in understanding how tumor cells hijack the BM niche to fuel their progression.

We also suggest that clinically targeting BMAT is very feasible. We observed bone-anabolic anti-sclerostin antibodies can reduce myeloma-induced bone disease in three mouse models [66] and also found that these antibodies decrease BMAT [67], thus signifying that bone-targeting therapies may also modulate BMAT and suggesting a second method of action for these therapies. Metformin has also been shown to decrease BMAT in obese, high-fat diet mice [8], which could be related to its potential effects on myeloma [68–70]. Inhibiting the "vicious cycle" between myeloma cells and osteoclasts that causes osteolysis has been transformative in clinical practice, and we foresee that targeting BMAs may prove to be a novel and similarly transformative approach to treating bone cancer. We envision that future studies with our 3D models will help define the bidirectional crosstalk between adipose and tumor cells to expose druggable targets, novel treatments, or disease and response biomarkers to change the course of myeloma.

5. Conclusion

We have developed a novel 3D co-culture model system of bone marrow adipose tissue and myeloma cells that allows for accurate *in vitro* recapitulation of adipocyte function and adipocyte-myeloma interaction. We demonstrated our ability to differentiate and sustain adipose tissue for long periods (3 months) on silk scaffolds and showed evidence that 3D BMAT is superior compared to 2D BMAT using microarray analyses. Our work identified autofluorescent lipids within adipocytes and showed that BMA lipids are reduced when co-cultured with myeloma cells. We found that many, but not all BM stromal cells are adipogenic progenitor cells. Our lab and others are now attempting to define and characterize the BM adipocyte progenitor cell and its cell surface markers, and compare this cell to the currently known multipotent stem cell defined with specific cell surface markers [71,72]. Identifying the BM adipocyte precursor, predicted to be a $Pref1^{+,}$ $RANKL^{+}$ precursor [73], and isolating that from the bulk BM stroma population is an interesting future direction beyond the scope of this work.

Supplementary data to this article can be found online at https://doi.org/10.1016/j.bone.2018.01.023.

Acknowledgements

Support was made possible by the Vermont Genetics Network Microarray and Bioinformatics Core Facilities through Grant Number 8P20GM103449 from the INBRE Program of the National Institute of General Medical Sciences (NIGMS) of the National Institutes of Health (NIH). The authors' work is also supported by the Tissue Engineering Resource Center, P41 EB002520, and by the confocal microscopy, physiology, and lipidomics and proteomics cores funded by the NIH/NIGMS grants U54GM115516, P30 GM106391, P20GM121301, and P30GM103392. The authors' work is supported by Start-up funds from the Maine Medical Center Research Institute (MMCRI), Maine Medical Center (MMC's) Biobank, the NIH/NIDDK (R24 DK092759-01), the NIH/NIAMS P30AR066261, and the American Cancer Society (Research Grant #IRG-16-191-33). The content is solely the responsibility of the authors and does not necessarily represent the official views of the NIH. We thank Drs. Igor Prudovsky and Anna Sitarski for help with imaging and the MMCRI Bioengineering Core for the silk scaffolds.

Disclosure statement

No competing financial interests exist.

References

[1] M. Styner, G.M. Pagnotti, K. Galior, X. Wu, W.R. Thompson, G. Uzer, B. Sen, Z. Xie, M.C. Horowitz, M.A. Styner, C. Rubin, J. Rubin, Exercise regulation of marrow fat in the setting of PPARγ agonist treatment in female C57BL/6 mice, Endocrinology 156 (2015) 2753–2761, https://doi.org/10.1210/en.2015-1213.

[2] C.R. Doucette, M.C. Horowitz, R. Berry, O.A. MacDougald, R. Anunciado-Koza, R.A. Koza, C.J. Rosen, A high fat diet increases bone marrow adipose tissue (MAT) but does not Alter trabecular or cortical bone mass in C57BL/6J mice, J. Cell. Physiol. 230 (2015) 2032–2037, https://doi.org/10.1002/jcp.24954.

[3] M.R. Reagan, C.J. Rosen, Navigating the bone marrow niche: translational insights and cancer-driven dysfunction, Nat. Rev. Rheumatol. 12 (2015) 154–168, https://doi.org/10.1038/nrrheum.2015.160.

[4] M.J. Devlin, A.M. Cloutier, N.A. Thomas, D.A. Panus, S. Lotinun, I. Pinz, R. Baron, C.J. Rosen, M.L. Bouxsein, Caloric restriction leads to high marrow adiposity and low bone mass in growing mice, J. Bone Miner. Res. 25 (2010) 2078–2088, https://doi.org/10.1002/jbmr.82.

[5] E.L. Scheller, Rosen, What's the matter with MAT? Marrow adipose tissue, metabolism, and skeletal health, Ann. N. Y. Acad. Sci. 1311 (2014) 14–30, https://doi.org/10.1111/nyas.12327.

[6] Z.S. Templeton, W.-R. Lie, W. Wang, Y. Rosenberg-Hasson, R.V. Alluri, J.S. Tamaresis, M.H. Bachmann, K. Lee, W.J. Maloney, C.H. Contag, B.L. King, Breast cancer cell colonization of the human bone marrow adipose tissue niche, Neoplasia 17 (2015) 849–861, https://doi.org/10.1016/j.neo.2015.11.005.

[7] B.J. Adler, K. Kaushansky, C.T. Rubin, Obesity-driven disruption of haematopoiesis and the bone marrow niche, Nat. Rev. Endocrinol. 10 (2014) 737–748, https://doi.org/10.1038/nrendo.2014.169.

[8] S. Bornstein, M. Moschetta, Y. Kawano, A. Sacco, D. Huynh, D. Brooks, S. Manier, H. Fairfield, C. Falank, A.M. Roccaro, K. Nagano, R. Baron, M. Bouxein, C. Vary, I.M. Ghobrial, C.J. Rosen, M.R. Reagan, Metformin affects cortical bone mass and marrow adiposity in diet-induced obesity in male mice, Endocrinology 158 (2017)https://doi.org/10.1210/en.2017-00299.

[9] J.M. Patsch, X. Li, T. Baum, S.P. Yap, D.C. Karampinos, A.V. Schwartz, T.M. Link, Bone marrow fat composition as a novel imaging biomarker in postmenopausal women with prevalent fragility fractures, J. Bone Miner. Res. 28 (8) (2013) 1721, https://doi.org/10.1002/jbmr.1950.

[10] R.M.A. Moysés, S.C. Schiavi, Sclerostin, osteocytes, and chronic kidney disease – mineral bone disorder, Semin. Dial. 28 (2015) 578–586, https://doi.org/10.1111/sdi.12415.

[11] M.J. Devlin, C.J. Rosen, The bone-fat interface: basic and clinical implications of marrow adiposity, Lancet Diabetes Endocrinol. 3 (2015) 141–147, https://doi.org/10.1016/S2213-8587(14)70007-5.

[12] S. Mostoufi-Moab, J. Magland, E.J. Isaacoff, W. Sun, C.S. Rajapakse, B. Zemel, F. Wehrli, K. Shekdar, J. Baker, J. Long, M.B. Leonard, Adverse fat depots and marrow adiposity are associated with skeletal deficits and insulin resistance in long-term survivors of pediatric hematopoietic stem cell transplantation, J. Bone Miner. Res. 30 (2015) 1657–1666, https://doi.org/10.1002/jbmr.2512.

[13] S. Urs, T. Henderson, P. Le, C.J. Rosen, L. Liaw, Tissue-specific expression of Sprouty1 in mice protects against high-fat diet-induced fat accumulation, bone loss and metabolic dysfunction, Br. J. Nutr. 108 (2012) 1025–1033, https://doi.org/10.1017/S0007114511006209.

[14] A.L. Hardaway, M.K. Herroon, E. Rajagurubandara, I. Podgorski, Bone marrow fat: linking adipocyte-induced inflammation with skeletal metastases, Cancer Metastasis Rev. 33 (2014) 527–543, https://doi.org/10.1007/s10555-013-9484-y.

[15] T.N. Trotter, J.T. Gibson, T.L. Sherpa, P.S. Gowda, D. Peker, Y. Yang, Adipocyte-lineage cells support growth and dissemination of multiple myeloma in bone, Am. J. Pathol. 186 (2016) 3054–3063, https://doi.org/10.1016/j.ajpath.2016.07.012.

[16] M.R. Reagan, L. Liaw, C.J. Rosen, I.M. Ghobrial, Dynamic interplay between bone and multiple myeloma: emerging roles of the osteoblast, Bone 75 (2015) 161–169, https://doi.org/10.1016/j.bone.2015.02.021.

[17] M.K. Herroon, E. Rajagurubandara, A.L. Hardaway, K. Powell, A. Turchick, D. Feldmann, I. Podgorski, Bone marrow adipocytes promote tumor growth in bone via FABP4-dependent mechanisms, Oncotarget 4 (2013) 2108–2123, https://doi.org/10.18632/oncotarget.1482.

[18] C. Falank, H. Fairfield, M.R. Reagan, Signaling interplay between bone marrow adipose tissue and multiple myeloma cells, Front. Endocrinol. (Lausanne) 7 (2016) 67, https://doi.org/10.3389/fendo.2016.00067.

[19] H. Fairfield, C. Falank, L. Avery, M.R. Reagan, Multiple Myeloma in the Marrow: Pathogenesis and Treatments, 2016https://doi.org/10.1111/nyas.13038.

[20] M.M.M. McDonald, H. Fairfield, C. Falank, M.R.M.R. Reagan, Adipose, bone, and myeloma: contributions from the microenvironment, Calcif. Tissue Int. 100 (2016) 433–448, https://doi.org/10.1007/s00223-016-0162-2.

[21] C. Falank, H. Fairfield, M. Farrell, M.R. Reagan, New bone cell type identified as driver of drug resistance in multiple myeloma: the bone marrow adipocyte, Blood 130 (2017) 122.

[22] I. Podgorski, B.E. Linebaugh, J.E. Koblinski, D.L. Rudy, M.K. Herroon, M.B. Olive, B.F. Sloane, Bone marrow-derived cathepsin K cleaves SPARC in bone metastasis, Am. J. Pathol. 175 (2009) 1255–1269, https://doi.org/10.2353/ajpath.2009.080906.

[23] W. Lu, W. Weng, Q. Zhu, Y. Zhai, Y. Wan, H. Liu, S. Yang, Y. Yu, Y. Wei, J. Shi, Small bone marrow adipocytes predict poor prognosis in acute myeloid leukaemia, Haematologica 103 (1) (2017) e21–e24 haematol. (173492) https://doi.org/10.3324/haematol.2017.173492.

[24] R.D. Abbott, R.Y. Wang, M.R. Reagan, Y. Chen, F.E. Borowsky, A. Zieba, K.G. Marra, P. Rubin, I.M. Ghobrial, D.L. Kaplan, J.P. Rubin, I.M. Ghobrial, D.L. Kaplan, The use of silk as a scaffold for mature, sustainable unilocular adipose 3D tissue engineered systems, Adv. Healthc. Mater. 5 (2016) 1667–1677, https://doi.org/10.1002/adhm.201600211.

[25] M.R. Reagan, Y. Mishima, S.V. Glavey, Y.Y. Zhang, S. Manier, Z.N. Lu, M. Memarzadeh, Y.Y. Zhang, A. Sacco, Y. Aljawai, J. Shi, Y. Tai, E. John, D.L. Kaplan, A.M. Roccaro, I.M. Ghobrial, J.E. Ready, D.L. Kaplan, A.M. Roccaro, I.M. Ghobrial, Investigating osteogenic differentiation in multiple myeloma using a novel 3D bone marrow niche model, Blood 124 (2014) 3250–3259, https://doi.org/10.1182/blood-2014-02-558007.

[26] U. Dadwal, C. Falank, H. Fairfield, S. Linehan, C.J. Rosen, D.L. Kaplan, J. Sterling, M.R. Reagan, Tissue-engineered 3D cancer-in-bone modeling: silk and PUR protocols, Bonekey Rep. 5 (2016), 842. https://doi.org/10.1038/bonekey.2016.75.

[27] N. Schutze, U. Noth, J. Schneidereit, C. Hendrich, F. Jakob, Differential expression of CCN-family members in primary human bone marrow-derived mesenchymal stem cells during osteogenic, chondrogenic and adipogenic differentiation, Cell Commun. Signal 3 (2005) 5, https://doi.org/10.1186/1478-811X-3-5.

[28] A. Swami, M.R. Reagan, P. Basto, Y. Mishima, N. Kamaly, S. Glavey, S. Zhang, M. Moschetta, D. Seevaratnam, Y. Zhang, J. Liu, M. Memarzadeh, J. Wu, S. Manier, J. Shi, N. Bertrand, Z.N. Lu, K. Nagano, R. Baron, A. Sacco, A.M. Roccaro, O.C. Farokhzad, I.M. Ghobrial, Engineered nanomedicine for myeloma and bone microenvironment targeting, Proc. Natl. Acad. Sci. U. S. A. 111 (2014) 10287–10292, https://doi.org/10.1073/pnas.1401337111.

[29] R. Oerlemans, N.E. Franke, Y.G. Assaraf, J. Cloos, I. van Zantwijk, C.R. Berkers, G.L. Scheffer, K. Debipersad, K. Vojtekova, C. Lemos, J.W. van der Heijden, B. Ylstra, G.J. Peters, G.L. Kaspers, B.A.C. Dijkmans, R.J. Scheper, G. Jansen, Molecular basis of bortezomib resistance: proteasome subunit beta5 (PSMB5) gene mutation and overexpression of PSMB5 protein, Blood 112 (2008) 2489–2499, https://doi.org/10.1182/blood-2007-08-104950.

[30] R.D. Abbott, R.Y. Wang, M.R. Reagan, Y. Chen, F.E. Borowsky, A. Zieba, K.G. Marra, J.P. Rubin, I.M. Ghobrial, D.L. Kaplan, The use of silk as a scaffold for mature, sustainable unilocular adipose 3D tissue engineered systems, Adv. Healthc. Mater. 5 (2016)https://doi.org/10.1002/adhm.201600211.

[31] Soley, Luna; Falank, Carolyne; Reagan, Michaela R. MicroRNA Transfer Between Bone Marrow Adipose and Multiple Myeloma Cells. Current osteoporosis reports 15(3):162-170. http://doi.org/10.1007/s11914-017-0360-5.

[32] M.R. Reagan, I.M. Ghobrial, Multiple myeloma mesenchymal stem cells: characterization, origin, and tumor-promoting effects, Clin. Cancer Res. 18 (2012)https://doi.org/10.1158/1078-0432.CCR-11-2212.

[33] M.R. Reagan, Y. Mishima, S.V. Glavey, Y. Zhang, S. Manier, Z.N. Lu, M. Memarzadeh, Y. Zhang, A. Sacco, Y. Aljawai, J. Shi, Y.-T. Tai, J.E. Ready, D.L. Kaplan, A.M. Roccaro, I.M. Ghobrial, Investigating osteogenic differentiation in multiple myeloma using a novel 3D bone marrow niche model, Blood 124 (2014)https://doi.org/10.1182/blood-2014-02-558007.

[34] M.R. Reagan, I.M. Ghobrial, Multiple myeloma-mesenchymal stem cells: characterization, origin, and tumor-promoting effects, Clin. Cancer Res. 18 (2012) 342–349, https://doi.org/10.1158/1078-0432.CCR-11-2212.

[35] B.M. Baker, C.S. Chen, Deconstructing the third dimension: how 3D culture microenvironments alter cellular cues, J. Cell Sci. 125 (2012) 3015–3024, https://doi.org/10.1242/jcs.079509.

[36] A.M. Sitarski, H. Fairfield, C. Falank, M.R. Reagan, 3D tissue engineered in vitro models of cancer in bone, ACS Biomater Sci. Eng. (2017) Ahead of Press, (Published Online: June 9, 2017) https://doi.org/10.1021/acsbiomaterials.7b00097.

[37] K.A. Fitzgerald, J. Guo, E.G. Tierney, C.M. Curtin, M. Malhotra, R. Darcy, F.J. O'Brien, C.M. O'Driscoll, The use of collagen-based scaffolds to simulate prostate cancer bone metastases with potential for evaluating delivery of nanoparticulate gene therapeutics, Biomaterials 66 (2015) 53–66, https://doi.org/10.1016/j.biomaterials.2015.07.019.

[38] T. Pan, E.L.S.S. Fong, M. Martinez, D.A. Harrington, S.-H. Lin, M.C. Farach-Carson, R.L. Satcher, Three-dimensional (3D) culture of bone-derived human 786-O renal cell carcinoma retains relevant clinical characteristics of bone metastases, Cancer Lett. 365 (2015) 89–95, https://doi.org/10.1016/j.canlet.2015.05.019.

[39] E.L.S. Fong, X. Wan, J. Yang, M. Morgado, A.G. Mikos, D.A. Harrington, N.M. Navone, M.C. Farach-Carson, A 3D in vitro model of patient-derived prostate cancer xenograft for controlled interrogation of in vivo tumor-stromal interactions, Biomaterials 77 (2015) 164–172, https://doi.org/10.1016/j.biomaterials.2015.10.059.

[40] A. Villasante, A. Marturano-Kruik, G. Vunjak-Novakovic, Bioengineered human tumor within a bone niche, Biomaterials 35 (2014) 5785–5794, https://doi.org/10.1016/j.biomaterials.2014.03.081.

[41] S.P. Pathi, C. Kowalczewski, R. Tadipatri, C. Fischbach, A novel 3-D mineralized tumor model to study breast cancer bone metastasis, PLoS One 5 (2010), e8849. https://doi.org/10.1371/journal.pone.0008849.

[42] C. Fischbach, R. Chen, T. Matsumoto, T. Schmelzle, J.S. Brugge, P.J. Polverini, D.J. Mooney, Engineering tumors with 3D scaffolds, Nat. Methods 4 (2007) 855–860, https://doi.org/10.1038/nmeth1085.

[43] Y.-H. Wang, J.-Y. Wu, P.-J. Chou, C.-H. Chen, C.-Z. Wang, M.-L. Ho, J.-K. Chang, M.-L. Yeh, C.-H. Chen, Characterization and evaluation of the differentiation ability of human adipose-derived stem cells growing in scaffold-free suspension culture, Cytotherapy 16 (2014) 485–495, https://doi.org/10.1016/j.jcyt.2013.07.015.

[44] H. Sugihara, N. Yonemitsu, S. Miyabara, S. Toda, Proliferation of unilocular fat cells in the primary culture, J. Lipid Res. 28 (1987) 1038–1045.

[45] H.H. Zhang, S. Kumar, A.H. Barnett, M.C. Eggo, Ceiling culture of mature human adipocytes: use in studies of adipocyte functions, J. Endocrinol. 164 (2000) 119–128.

[46] J. Shen, A. Sugawara, J. Yamashita, H. Ogura, S. Sato, Dedifferentiated fat cells: an alternative source of adult multipotent cells from the adipose tissues, Int. J. Oral Sci. 3 (2011) 117–124, https://doi.org/10.4248/IJOS11044.

[47] H. Sugihara, N. Yonemitsu, S. Miyabara, K. Yun, Primary cultures of unilocular fat cells: characteristics of growth in vitro and changes in differentiation properties, Differentiation 31 (1986) 42–49.

[48] O.A. MacDougald, C.S. Hwang, H. Fan, M.D. Lane, Regulated expression of the obese gene product (leptin) in white adipose tissue and 3T3-L1 adipocytes, Proc. Natl. Acad. Sci. U. S. A. 92 (1995) 9034–9037.

[49] R. Bouillon, G. Carmeliet, L. Lieben, M. Watanabe, A. Perino, J. Auwerx, K. Schoonjans, A. Verstuyf, Vitamin D and energy homeostasis: of mice and men, Nat. Rev. Endocrinol. 10 (2014) 79–87, https://doi.org/10.1038/nrendo.2013.226.

[50] M. Serlachius, L.C. Andersson, Upregulated expression of stanniocalcin-1 during adipogenesis, Exp. Cell Res. 296 (2004) 256–264, https://doi.org/10.1016/j.yexcr.2004.02.016.

[51] Z. Peng, Z. Dong, Q. Chang, W. Zhan, Z. Zeng, S. Zhang, F. Lu, Tissue engineering chamber promotes adipose tissue regeneration in adipose tissue engineering models through induced aseptic inflammation, Tissue Eng. Part C Methods 20 (2014) 875–885, https://doi.org/10.1089/ten.TEC.2013.0431.

[52] W. Liu, X. Yang, X. Yan, J. Cui, W. Liu, M. Sun, Y. Rao, F. Chen, Directing parthenogenetic stem cells differentiate into adipocytes for engineering injectable adipose tissue, Stem Cells Int. 2014 (2014), 423635. https://doi.org/10.1155/2014/423635.

[53] G.H. Altman, F. Diaz, C. Jakuba, T. Calabro, R.L. Horan, J. Chen, H. Lu, J. Richmond, D.L. Kaplan, Silk-based biomaterials, Biomaterials 24 (2003) 401–416.

[54] H.S.H.J. Kim, U.-J. Kim, H.S.H.J. Kim, C. Li, M. Wada, G.G. Leisk, D.L. Kaplan, Bone tissue engineering with premineralized silk scaffolds, Bone 42 (2008) 1226–1234, https://doi.org/10.1016/j.bone.2008.02.007.

[55] Y. Wang, D.D. Rudym, A. Walsh, L. Abrahamsen, H.S.H.-J.H.S. Kim, H.S.H.-J.H.S. Kim, C. Kirker-Head, D.L. Kaplan, In vivo degradation of three-dimensional silk fibroin scaffolds, Biomaterials 29 (2008) 3415–3428, https://doi.org/10.1016/j.biomaterials.2008.05.002.

[56] J.M. Page, A.R. Merkel, N.S. Ruppender, R. Guo, U.C. Dadwal, S.A. Cannonier, S. Basu, S.A. Guelcher, J.A. Sterling, Matrix rigidity regulates the transition of tumor cells to a bone-destructive phenotype through integrin β3 and TGF-β receptor type II, Biomaterials 64 (2015) 33–44, https://doi.org/10.1016/j.biomaterials.2015.06.026.

[57] N.S. Ruppender, A.R. Merkel, T.J. Martin, G.R. Mundy, J.A. Sterling, S.A. Guelcher, Matrix rigidity induces osteolytic gene expression of metastatic breast cancer cells, PLoS One 5 (2010), e15451. https://doi.org/10.1371/journal.pone.0015451.

[58] M.K. Herroon, J.D. Diedrich, I. Podgorski, New 3D-culture approaches to study interactions of bone marrow adipocytes with metastatic prostate cancer cells, Front. Endocrinol. (Lausanne) 7 (2016), 84. https://doi.org/10.3389/fendo.2016.00084.
[59] T.K. Schuessler, X.Y. Chan, H.J. Chen, K. Ji, K.M. Park, A. Roshan-Ghias, P. Sethi, A. Thakur, X. Tian, A. Villasante, I.K. Zervantonakis, N.M. Moore, L.A. Nagahara, N.Z. Kuhn, Biomimetic tissue-engineered systems for advancing cancer research: NCI Strategic Workshop report, Cancer Res. 74 (2014) 5359–5363, https://doi.org/10.1158/0008-5472.CAN-14-1706.
[60] S.Y. Pan, K.C. Johnson, A.-M. Ugnat, S.W. Wen, Y. Mao, Association of obesity and cancer risk in Canada, Am. J. Epidemiol. 159 (2004) 259–268.
[61] A. Wallin, S.C. Larsson, Body mass index and risk of multiple myeloma: a meta-analysis of prospective studies, Eur. J. Cancer 47 (2011) 1606–1615, https://doi.org/10.1016/j.ejca.2011.01.020.
[62] R. Islam, K. Altundag, M. Kurt, O. Altundag, S. Turen, Association between obesity and multiple myeloma in postmenopausal women may be attributed to increased aromatization of androgen in adipose tissue, Med. Hypotheses 65 (2005) 1001–1002, https://doi.org/10.1016/j.mehy.2005.05.014.
[63] J.E. Reseland, S. Reppe, O.K. Olstad, H. Hjorth-Hansen, A.T. Brenne, U. Syversen, A. Waage, P.O. Iversen, Abnormal adipokine levels and leptin-induced changes in gene expression profiles in multiple myeloma, Eur. J. Haematol. 83 (2009) 460–470, https://doi.org/10.1111/j.1600-0609.2009.01311.x.
[64] J. Caers, S. Deleu, Z. Belaid, H. De Raeve, E. Van Valckenborgh, E. De Bruyne, M.-P. Defresne, I. Van Riet, B. Van Camp, K. Vanderkerken, Neighboring adipocytes participate in the bone marrow microenvironment of multiple myeloma cells, Leukemia 21 (2007) 1580–1584, https://doi.org/10.1038/sj.leu.2404658.
[65] Z. Liu, J. Xu, J. He, H. Liu, P. Lin, X. Wan, N.M. Navone, Q. Tong, L.W. Kwak, R.Z. Orlowski, J. Yang, M. Nora, Q. Tong, L.W. Kwak, R.Z. Orlowski, J. Yang, Mature adipocytes in bone marrow protect myeloma cells against chemotherapy through autophagy activation, Oncotarget 6 (2015) 34329–34341, https://doi.org/10.18632/oncotarget.6020.
[66] M.M. McDonald, M.R. Reagan, S.E. Youlten, S.T. Mohanty, A. Seckinger, R.L. Terry, J.A. Pettitt, M.K. Simic, T.L. Cheng, A. Morse, L.M.T. Le, D. Abi-Hanna, I. Kramer, C. Falank, H. Fairfield, I.M. Ghobrial, P.A. Baldock, D.G. Little, M. Kneissel, K. Vanderkerken, J.H.D. Bassett, G.R. Williams, B.O. Oyajobi, D. Hose, T.G. Phan, P.I. Croucher, Inhibiting the osteocyte-specific protein sclerostin increases bone mass and fracture resistance in multiple myeloma, Blood 129 (2017)https://doi.org/10.1182/blood-2017-03-773341.
[67] H. Fairfield, C. Falank, E. Harris, V. Demambro, M. McDonald, J.A. Pettitt, S.T. Mohanty, P. Croucher, I. Kramer, M. Kneissel, C.J. Rosen, M.R. Reagan, The skeletal cell-derived molecule sclerostin drives bone marrow adipogenesis, J. Cell. Physiol. 233 (2017) 1156–1167, https://doi.org/10.1002/jcp.25976.
[68] F.-M. Zi, J.-S. He, Y. Li, C. Wu, L. Yang, Y. Yang, L.-J. Wang, D.-H. He, Y. Zhao, W.-J. Wu, G.-F. Zheng, X.-Y. Han, H. Huang, Q. Yi, Z. Cai, Metformin displays anti-myeloma activity and synergistic effect with dexamethasone in in vitro and in vivo xenograft models, Cancer Lett. 356 ((2015) 443–453, https://doi.org/10.1016/j.canlet.2014.09.050.
[69] S. Jagannathan, M.A.Y.A. Malek, E. Malek, N. Vad, T. Latif, K.C. Anderson, J.J. Driscoll, Pharmacologic screens reveal metformin that suppresses GRP78-dependent autophagy to enhance the anti-myeloma effect of bortezomib, Leukemia (2015)https://doi.org/10.1038/leu.2015.157.
[70] S.-H. Chang, S. Luo, K.K. O'Brian, T.S. Thomas, G.A. Colditz, N.P. Carlsson, K.R. Carson, Association between metformin use and transformation of monoclonal gammopathy of undetermined significance to multiple myeloma in U.S. veterans with diabetes mellitus: a population-based cohort study, Lancet. Haematol. 2 (2015) e30–e36, https://doi.org/10.1016/S2352-3026(14)00037-4.
[71] H. Wang, F. Cao, A. De, Y. Cao, C. Contag, S.S. Gambhir, J.C. Wu, X. Chen, Trafficking mesenchymal stem cell engraftment and differentiation in tumor-bearing mice by bioluminescence imaging, Stem Cells 27 (2009) 1548–1558, https://doi.org/10.1002/stem.81.
[72] M. Dominici, K. Le Blanc, I. Mueller, I. Slaper-Cortenbach, F. Marini, D. Krause, R. Deans, A. Keating, D. Prockop, E. Horwitz, Minimal criteria for defining multipotent mesenchymal stromal cells. The International Society for Cellular Therapy position statement, Cytotherapy 8 (2006) 315–317, https://doi.org/10.1080/14653240600855905.
[73] Y. Fan, J. Hanai, P.T. Le, R. Bi, D. Maridas, V. DeMambro, C.A. Figueroa, S. Kir, X. Zhou, M. Mannstadt, R. Baron, R.T. Bronson, M.C. Horowitz, J.Y. Wu, J.P. Bilezikian, D.W. Dempster, C.J. Rosen, B. Lanske, Parathyroid hormone directs bone marrow mesenchymal cell fate, Cell Metab. 25 (2017) 661–672, https://doi.org/10.1016/j.cmet.2017.01.001.